Check for updates

Remove hydrogen and store it too: an acid-in-clay based electro-chemical solution†

Kyung-Shik Kim,[a] Jin-Sung Park,[b] Young-Chul Yoon,[cd] Jinwoo Kim, [iD][c] Ju Li, [iD] *[ab] Bilge Yildiz [iD] *[ab] and Cemal Cem Tasan*[a]

Extracting hydrogen from metallic components can open up a new pathway for preventing hydrogen embrittlement. To this end, we propose an electrochemically driven, all-solid method for hydrogen control, capable of both extracting and storing hydrogen simultaneously. In this approach, we employ acid-in-clay as a proton conducting electrolyte at room temperature. Through this electrochemical treatment, hydrogen is efficiently extracted from precharged steels, thereby restoring their tensile properties and preventing embrittlement. Moreover, it has been confirmed that the extracted hydrogen can be efficiently collected at the counter electrode, demonstrating the significant advantages of the process.

New concepts

As efforts to establish a hydrogen energy economy intensify, increasing attention has been paid to infrastructure development and advancements in hydrogen storage techniques. However, hydrogen embrittlement remains a critical challenge for structural components in the hydrogen economy and various other key industries. While most research targets the development of hydrogen-resistant alloys, we present an alternative solution to mitigate hydrogen embrittlement in existing infrastructures while simultaneously storing hydrogen. Our novel acid-in-clay based electrochemical method, applied to the surface of metallic components, effectively extracts internal hydrogen and restores the tensile properties. The extracted hydrogen is transferred through an acid-in-clay solid electrolyte as protons, which are then reduced at the counter electrode and diffused into it with 74% efficiency. This process not only prevents hydrogen embrittlement in essential metallic alloys across diverse industries but also contributes to hydrogen storage for future energy use. Furthermore, the simplicity and flexibility of this process enhances its adaptability to various operational conditions, making it a scalable and versatile solution. Optimizing this methodology by exploring other solid electrolytes and hydrogen storage materials can lead to further improvements and broader implementation.

Introduction

Hydrogen embrittlement (HE) is a key issue for numerous structural components in energy and transportation industries, which rely on the use of high-strength alloys. In such alloys, hydrogen (H) can be inadvertently introduced from various sources, leading to unpredictable failures, as reported for steels,[1–3] aluminium alloys,[4,5] titanium alloys,[6,7] nickel alloys,[8] and others.[9–13] Stopping H uptake entirely is challenging due to the abundance of opportunities metals "face" hydrogen during processing (e.g., during welding[14] or coating[15]), or use (e.g., from refrigerating systems in nuclear reactors[9,10] and from transported H in pipelines[16]). Note that, due to the emergence of H-economy,[17] the number of engineering components operating in H-rich environments will inevitably be further increasing. As solutions, where possible, applying H-barrier coatings can prevent H ingress;[18] and relief heat treatments can accelerate H desorption.[19] However, the most common strategy to prevent HE is simply choosing (or where possible, designing) alloys that show low susceptibility for HE.[20] Unfortunately, this solution effectively excludes the engineering use of numerous high-strength alloys (i.e. with tensile strength above 1 GPa) in H relevant applications.[21]

An important point regarding all these preventive approaches is the fact that they are all "global" solutions. That is, these solutions rely on an underlying assumption that the risk of HE is equal across the entire volume of a component, regardless of the local conditions. However, engineering practice, and the large body of fundamental investigations have demonstrated that HE occurs only when certain conditions of mechanical stress, microstructure and H concentration are simultaneously satisfied.[22] Such high-risk conditions include,

[a] Department of Materials Science and Engineering, Massachusetts Institute of Technology, 77 Massachusetts Avenue, Cambridge, MA 02139, USA. E-mail: liju@mit.edu, byildiz@mit.edu, tasan@mit.edu

[b] Department of Nuclear Science and Engineering, Massachusetts Institute of Technology, 77 Massachusetts Avenue, Cambridge, MA 02139, USA

[c] Energy Materials Research Center, Korea Institute of Science and Technology, Seoul 02792, Republic of Korea

[d] Department of Materials Science and Engineering, Seoul National University, Seoul 08826, Republic of Korea

† Electronic supplementary information (ESI) available. See DOI: https://doi.org/10.1039/d4mh01071j
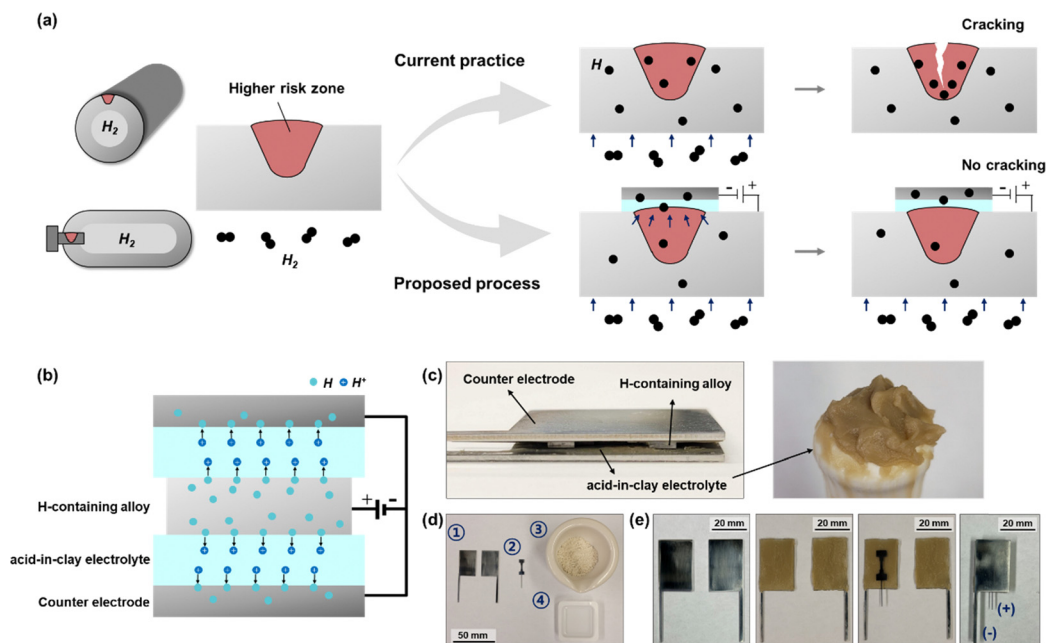
Fig. 1 Illustration of the electrochemically stimulated desorption (ECD) system. (a) Schematic representation of the proposed, preventive maintenance procedure of ECD, for hypothetical transport or storage applications. (b) Schematic drawing depicting the ECD setup. (c) Actual image of the setup (left), and a higher magnification view of the electrolyte (right). (d) Images displaying the components for ECD: ① counter electrode (304 stainless steel), ② tensile sample (working electrode, 430 stainless steel), ③ sepiolite clay powder, and ④ phosphoric acid. (e) The step-by-step process of preparation for the ECD treatment.

for example, zones of high residual stress[23] (e.g., weld zones[14,24]), and zones exposed to low temperatures[25] or high external stresses.[26] This is schematically demonstrated in Fig. 1(a). Once H uptake or internal diffusion leads to the critical H content in a high-risk zone of an engineering component, micro-cracks are nucleated. This, in-turn, leads to more H diffusion to the micro-crack tip and further crack growth towards catastrophic failure.

"Local" solutions that focus on lowering the possibility of HE only in such high-risk regions could realize HE prevention at lower effort and cost, and provide significantly increased flexibility in material selection, coating application, systems design, and operation conditions. To this end, accelerating local H desorption by electro-chemical extraction of H has the potential to be a highly effective approach. This approach, however, has been largely neglected due to the lack of a fundamental understanding, and of a feasible methodology. Building on a liquid-cell proof-of-principle study,[27,28] in this work, we introduce an advanced, all-solid-state methodology which utilizes a proton-conducting electrolyte, and demonstrate the effectiveness of this method in preventing HE.

Proton-conducting solid electrolytes (SEs) have been investigated for the development of proton batteries and hydrogen fuel cells in recent years.[29,30] Among candidates such as Nafion,[31,32] polybenzimidazole (PBI),[31,33] heteropoly acids (HPA),[31,34] metal–organic frameworks (MOF),[35] covalent organic frameworks (COF),[36] and polymers;[37] acid-in-clay electrolytes stand out due to their outstanding proton conductivity, durability, and wide operation windows.[38] The sepiolite–phosphoric acid-distilled water system, employed in the current work, exhibits the highest proton conductivity among various acid-in-clay systems, reaching

up to 15 mS cm^{-1} at 25 °C.[38] Also, sepiolite clay has a highly porous structure and significant surface area exhibiting the highest Brunauer–Emmett–Teller (BET) surface area measurement of 112.9 m^2 g^{-1}, which is higher than those of other types of clays.[38] Finally, this electrolyte can be easily applied on the surface of the metal as a paste, allowing a conformal coating on the surface of the metal components. It should be noted that referring the acid-in-clay as a 'solid' is sometimes debated due to the presence of water. Here, our decision is based on the in situ cryogenic XRD results from our previous paper revealing a lower chemical potential of water inside acid-in-clay than that of bulk liquid water.[38]

The preventive solution of the proposed methodology is demonstrated schematically in Fig. 1(a). Instead of replacing components that exhibit micro-cracking regularly (which leads to high maintenance and service down-time costs),[39] the proposed process of applying electrochemical H desorption allows prevention of HE by extracting H from the system. While different application strategies are possible due to its simplicity, flexibility, and cost-effectiveness; the clearest use cases involve short-duration H extraction during manufacturing (e.g., upon welding), or during use (e.g., high-risk locations in the existing infrastructure). The cost-effectiveness of this solution is worth mentioning: using gas pipelines as a specific example, the additional cost of the alternative solution, i.e., having pipelines with H barrier coatings, is projected to range from up to 6.5 percent of the overall construction expenses.[40,41] On the other hand, this electrolyte: (i) is more cost effective in terms of material costs compared to potential coating materials (as well as compared to other solid electrolytes);[42,43] (ii) can be

directly applied, on-site, to the external surface of pipelines (avoiding, *e.g.*, the necessity for the costly pre-processing steps needed for coating applications, and reinstallation costs), wherever and whenever needed. Additionally, H loss can be minimized since the extracted H during electrochemical desorption can be stored and reused (see below).

In this study, we used two types of commercial grade steels, a 430 stainless steel (ASTM A240) and a low-carbon steel (ASTM A109), for the verification of an electrochemically stimulated desorption (ECD) system using a sepiolite clay-based electrolyte (illustrated in Fig. 1(b)–(e)). A 430 stainless steel (430SS) was selected for comparison with the proof-of-principle study involving a liquid electrolyte,[27] while a low-carbon steel having a ferritic + pearlitic microstructure (Fig. S1a, ESI†) was chosen to assess the applicability to pipeline steels.[44] Tensile properties and fracture characteristics were investigated in relation to the H content within the steel samples.

Results

The results of tensile testing for all the conditions subjected to H charging and ECD treatments are summarized in Fig. 2(a)–(d), and Tables S1, S2 in the ESI.† For 430SS, H was charged electrochemically for 30 minutes to validate the degree of HE. Note that electrochemical charging is a severe way of introducing H compared to pressurized H gas charging (as in real applications for H gas pipelines).[45] Synchrotron XRD results demonstrated that the lattice parameter and strain levels remained within the standard deviation upon two hours of electrochemical H charging, revealing a negligible charging effect on the steels in the absence of deformation (Fig. S2, ESI†). While the as received 430SS exhibited a tensile ductility of 38%, H charging reduced it to 20% (Fig. 1(a) and Table S1, ESI†). Yield strength, on the other hand, increased from 314 MPa to 338 MPa due to the strengthening effect of interstitial H.[46,47] To investigate H desorption in an
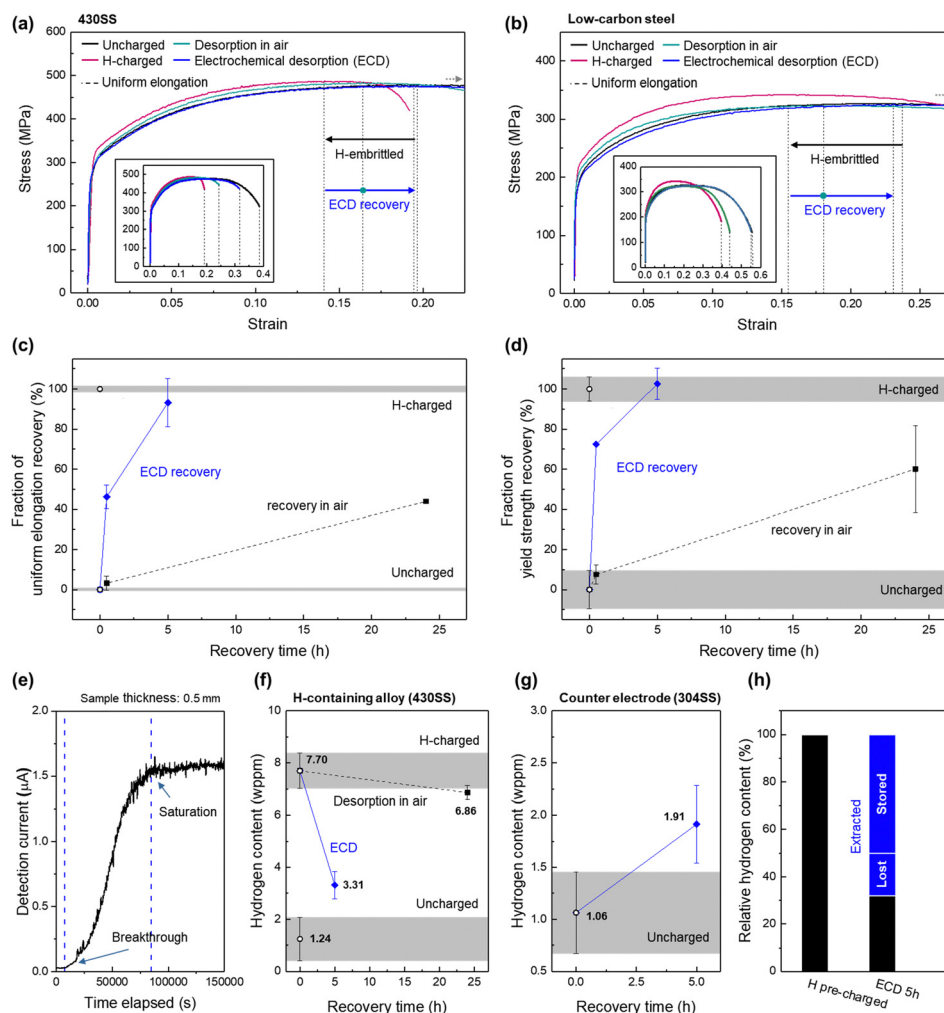

Fig. 2 Results of tensile testing and hydrogen measurement for each test condition. Engineering strain−stress curves of the as-received and H pre-charged samples overlapped with samples exposed to air after H charging, and after ECD treatment for (a) 430 stainless steel and (b) low-carbon steel. (c) Fraction of uniform elongation recovery for all conditions with respect to the recovery time for the 430 stainless steel. (d) Fraction of yield strength recovery for all conditions with respect to the recovery time for the 430 stainless steel. (e) Hydrogen permeation test results for the 430 stainless steel. (f) H content (wppm) after each test condition for the target metal (430 stainless steel) and the (g) counter electrode (304 stainless steel). (h) Ratio of the H content after H charging and after five hours of ECD treatment.

ambient environment, the H-charged tensile samples were tested after exposure to air for 30 minutes and 24 hours. The tensile results after 30 minutes of exposure in air were almost the same as the one tested without delay, indicating that the "natural" H desorption was negligible. The tensile properties showed some recovery when the exposure time was increased to 24 hours, as the fracture elongation changed back from 19.5% to 24.3%, and yield strength from 338 MPa to 324 MPa. However, the deviation from the as-received state remained significant. ECD treatment, on the other hand, accelerated the recovery of the tensile properties. Just 30 minutes of the electrochemical desorption treatment already achieved similar tensile properties to those of the one exposed in air for 24 hours. After five hours of ECD treatment, the yield strength and uniform elongation were fully recovered to their initial state (Fig. 2(c), (d) and Table S1, ESI†). Nevertheless, it is important to highlight that the post-necking elongation did not fully recover. This would not be critical for most engineering applications, since reaching the point of necking is already a sufficient reason for replacement in most cases. That stated, we will delve into the scientific aspects of this in the subsequent discussions.

Low-carbon steel on the other hand exhibited an even more favourable behaviour upon the ECD treatment (Fig. 2(b) and Table S2, ESI†). In this case, the loss of tensile elongation owing to the H pre-charging was not as severe in the first place (compared to 430SS), as it retained 71% of the elongation even after one hour of H charging. As in the case of 430SS, natural desorption of H in air hardly recovered the tensile properties of this material: one hour exposure to air prior to tensile testing exhibited similar tensile ductility to that of the directly tested sample, and 24 hours of exposure could only achieve 78% of the initial elongation. In contrast, just one hour of ECD already led to 95% of the initial tensile ductility, and this increased to 96%

with five hours of ECD. Unlike the case of the 430 stainless steel, post-elongation also showed a full recovery. Further investigation of ECD provided below is focused on 430SS, since this provides opportunities to discuss potential improvements to the methodology.

To investigate the level of H extracted using ECD, we carried out further analyses. The effective H diffusivity of the employed 430SS measured from the H permeation test was 3.44×10^{-12} m^2 s^{-1}, which yields a H diffusion depth of around 111 μm from the surface by 30 minutes of H charging (Fig. 2(e)). This is around 41.6% of the initial gauge cross-section area. Hence, while 30 minutes were clearly not sufficient for H to diffuse all the way through the sample thickness, it could still decrease the fracture elongation to half from the initial value, showing typical HE. The quantitative H analysis results show that 1.24 wppm of H was already present in the non-treated state, and it increases up to 7.70 wppm upon H charging (Fig. 2(f) and Table S1, ESI†). After 24 hours of air exposure, 87% of pre-charged H was still inside the sample. This shows that the H desorption in an ambient environment is not effective even though H diffusivity is reported to be the highest in BCC, compared to FCC and HCP.[48] ECD treatment of five hours reduced the amount of H to 3.31 wppm. Interestingly, even though this is 32% of the charged H residing inside the tensile sample, the recovery of the tensile properties after five hours of ECD shows that most of the H responsible for property deterioration was extracted from the sample.

Distinct features of hydrogen-induced degradation and recovery through ECD treatment are readily observable on the fracture surface (Fig. 3). Fig. 3(a)–(d) illustrate the fracture mode within the gauge cross-section along with the corresponding H distribution. The uncharged sample exhibited a classical ductile fracture with dimples on the fracture surface
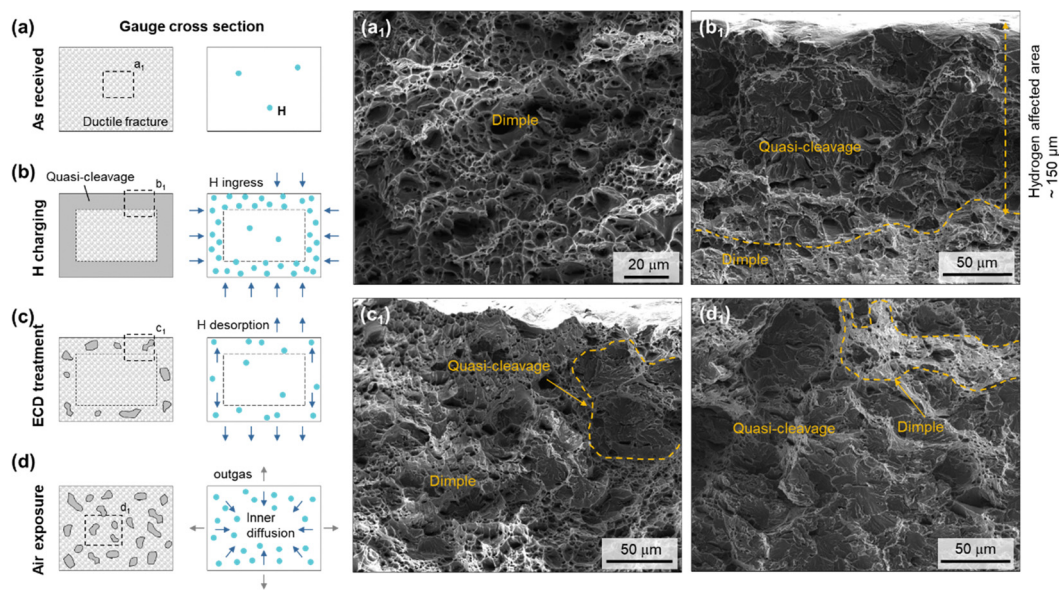

Fig. 3 Fractography and hydrogen distribution after each treatment. (a) As received sample with (a$_1$) fracture surface showing ductile fracture. (b) Hydrogen pre-charged sample showing (b$_1$) quasi-cleavage fracture in the H affected area. (c) ECD treated for five hours showing (c$_1$) a mixed fracture mode of ductile and quasi-cleavage fracture. (d) Hydrogen pre-charged and exposed to air for 24 hours also showing (d$_1$) a mixed fracture mode.

(Fig. 3(a) and (a$_1$)), indicating that the pre-existing H of 1.24 wppm (Fig. 2(f) and Table S1, ESI†) was not enough to induce embrittlement. With H pre-charging, quasi-cleavage fracture could be observed at H-affected regions, which was up to ~150 μm from the surfaces (Fig. 3(b) and (b$_1$)). The observed H-affected region depth was deeper than the calculated H diffusion depth from the measured diffusivity (111 μm) (Fig. 2(e)). The observed deviation is likely to originate from the diffusion of H during plastic deformation.[49,50] Since the entire sample was immersed into the electrolyte during H charging, the whole surface of the gauge was equally affected by H. With 30 minutes of ECD treatment, the fracture mode in the top and bottom areas (where there was contact with the electrolyte) became partially ductile, showing a mixture of dimples and quasi-cleavage fracture features (Fig. S3a and a$_1$, ESI†). The sides which had no contact with the electrolyte still showed quasi-cleavage fracture (Fig. S3a and a$_2$, ESI†). Increasing the ECD process to five hours induced a larger portion of the ductile failure region (Fig. 3(c), (c$_1$) and Fig. S3b, ESI†). Even the side region showed ductile fracture, indicating that ECD was effective in extracting H from the whole sample thickness (Fig. S3b$_1$, ESI†). These two ECD results indicate that H-diffusion is sensitive to the boundary conditions, and strongly promoted by the H concentration gradient introduced by the active ECD at the contacted area. Samples exposed to air before tensile testing were expected to exhibit a shallower H-affected region since H would have diffused out during this delay. However, surprisingly, traces of brittle fracture could be seen even in the center region of the gauge (Fig. 3(d) and (d$_1$)). This implies that H not only diffused out from the sample, but also diffused in the "opposite direction", *i.e.*, into the bulk of the sample. This process of H internal distribution likely contributes to the requirement of the longer H desorption duration, resulting in the aforementioned slower recovery of the tensile properties. In contrast, the internal diffusion and distribution of H were not prominent in the case of ECD-treated samples, because H desorption was driven directionally by an electrochemical potential difference applied across the ECD cell.

To study the contact conditions between the electrolyte and the tested samples, we fine-polished a 430SS sample (finishing with the colloidal silica step) and investigated the change in the height profile after ECD treatment. Five hours of ECD treatment induced a negligible change here, revealing the maximum deviation of 38 nm. This demonstrated that there was minimal removal of the steel during this process (Fig. S4b and c, ESI†). This limited material removal process led to reduced roughness from 21.1 nm (S_a, arithmetical mean height, ISO 25178),[51] to 20.7 and to 19.6 after 0.5 h and 5 h of ECD, respectively (Fig. S4a, ESI†). This is not surprising given the similarities with electrochemical polishing, where the sample is also set as the anode (positive potential) and the counter electrode as the cathode (negative potential). Next, to investigate the extreme case, the sample was kept in contact with the electrolyte for 24 hours, but without any electrical connections. The contact of the electrolyte and sample surface can be tracked due to the slight etching and pitting influence of the electrolyte on the steel (Fig. S5, ESI†), which created shallow surface variations between 100 nm and 350 nm (Fig. S5c, ESI†). Note that this etching effect left the overall roughness of the metal sample still at only 91.5 nm (S_a), suggesting limited mechanical consequences (Fig. S5a, ESI†). Importantly, these affected zones were not uniform throughout the surface, suggesting that the contact conditions were far from optimized. This effectively means that the reported success in property recovery (Fig. 2(a)) can even be further improved, simply by improving the surface contact conditions. Finally, the stability of the acid-in-clay should be mentioned. A freshly mixed acid-in-clay had a resistance of 269 ± 74 Ω, whereas exposing it in air for 24 h increased the resistance to 2804 ± 455 Ω (measured using the 4-point probe method). The intended applications do not necessitate such extended exposures, thus, this decrease in proton conductivity would be less during a typical ECD treatment. Nevertheless, it is important to note that the setup time should be controlled, also considering the etching during contact.

Analysis of surface damage resulting from deformation was also conducted on the fractured sample surfaces (Fig. 4 and Fig. S6, ESI†). As shown in Fig. S6a (ESI†), the as-received alloy fractured with necking, and no surface cracks were observed near the fractured region (Fig. 4(a) and (a$_1$)). When the sample was pre-charged with H, the necking became negligible and
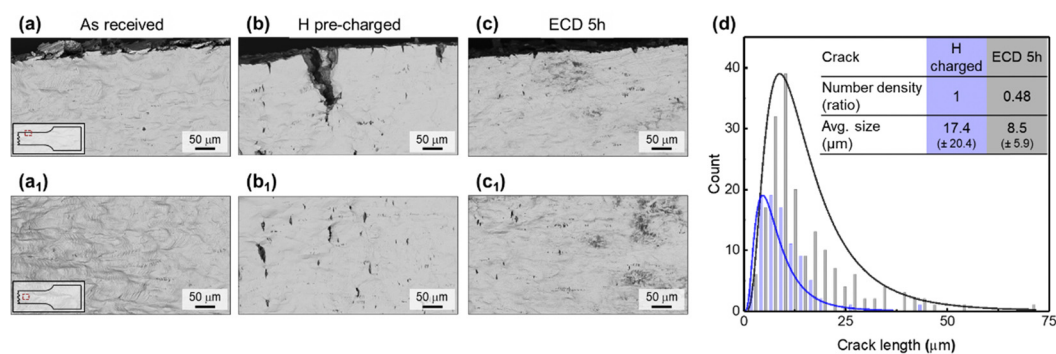

Fig. 4 Damage analysis of fractured tensile specimens. (a) Side surface view of the as-received sample near the fracture at one edge, and (a$_1$) in the inner region. (b), (b$_1$) Hydrogen pre-charged sample. (c), (c$_1$) ECD treated for five hours. (d) Number density and size of the cracks within 750 μm from the fracture surface.

Crack	H charged	ECD 5h
Number density (ratio)	1	0.48
Avg. size (μm)	17.4 (± 20.4)	8.5 (± 5.9)

abundant cracks were forming in the deformed region adjacent to the major crack which fractured (Fig. 4(b), (b₁) and Fig. S6b, ESI†). These cracks are all transgranular cracks which correspond to the quasi-cleavage fracture observed in the fracture surfaces (Fig. 3(b₁) and Fig. S7a, ESI†). With ECD treatment prior to tensile testing, the number density and size of these cracks decreased, and necking could be observed again (Fig. 4(c), (c₁) and Fig. S6c, ESI†). Both the number density and average size of the cracks decreased to half from the H charged condition when five hours of ECD treatment were applied (Fig. 4(d)). These small cracks are responsible for the quasi-cleavage traces in the fracture surface (Fig. 3(c₁) and Fig. S7b, ESI†).

Discussion

The proposed solid-state ECD system, utilizing an acid-in-clay proton electrolyte, demonstrated effective removal of H from the H-charged steels. However, it should be noticed that the recovery process in this H extraction approach is dependent on the specific constituents present in the steel microstructure. The presence of different H trapping sites and diffusion pathways may influence the level of HE and the recovery achieved by applying the ECD solution. In the two steels studied here, for example, full recovery of the total elongation was successfully achieved in the low-carbon steel. The post-uniform elongation of the stainless steel, on the other hand, was not fully recovered. While the engineering relevance of this limitation may not be significant, it is still important to discuss the underlying causes, to identify potential enhancements in the methodology.

When the data of H desorption are carefully studied in this case, it can be seen that 68% of H was extracted from the 430SS sample after five hours of the ECD operation (Table S1, ESI†). This amount is lower than that of the previously reported liquid based ECD approach, where 80% of H was removed from the sample. In that case, the fracture elongation was fully recovered.[27] The primary factor impeding complete recovery can be attributed to the HE mechanism in commercial 430SS, wherein carbides embedded in the ferritic microstructure play a significant role. The H trapping energy at carbides in 430SS is reported to be 2.4 times higher than that at the ferrite lattice.[52] It is reported that HE occurs through the process of micro-crack nucleation at these carbides with trapped H, which later propagate through the ferrite grains.[52] Such a mechanism was not observed for the low-carbon steel tested in this study, which may have contributed to the favourable response to ECD treatment.[53] Precipitates with a similar morphology can be observed within the ferritic matrix of 430SS studied here (Fig. S1b and c, ESI†). Given the unoptimized surface contact conditions between the electrolyte and the steel, here it is likely that some of the carbides with trapped H ended up remaining in those areas with weaker contact with the electrolyte. Such a micro-cracking phenomenon would explain the presence of local quasi-cleavage morphologies present in the fracture surfaces (Fig. 3(c₁)). Note that most such micro-cracks do not grow until necking (Fig. S6c, ESI†), and hence, create no significant effect on the uniform elongation (Fig. 2(a)). The absence of such an effect when employing a liquid electrolyte[27] is understandable, since the contact conditions in that case are more trivial to optimize. This, however, does not constitute an intrinsic limitation to the current H desorption solution, since applying more uniform pressure can improve the true contact area between the layers and reduce the local current density with the metallic alloys.[54]

The transfer of the extracted H is also worth discussing. For liquid based ECD, H within the metal can be extracted as protons, migrating through the alkaline liquid electrolyte, and ultimately undergoing reduction at the Pt counter electrode to evolve into H_2 bubbles.[27] The acid-in-clay electrolyte employed in the current methodology is also serving as a pathway for the protons extracted from the metal,[38] and migrate the protons to the 304 stainless steel (304SS) counter electrode where they are reduced. It is important to note that an austenitic steel was intentionally employed as the counter electrode in this study rather than Pt. This is due to the fact that the former has a higher possibility of H to diffuse into the steel rather than to form H_2 gas at the interface, which can be unfavourable in terms of surface contact. To verify this point, the H content inside the counter electrode was measured after five hours of ECD (Fig. 2(g) and (h)). The quantitative H analysis showed that the H content decreased by 4.39 wppm in the 430SS target metal, and increased by 0.85 wppm in the 304SS counter electrode. Considering that the weight ratio of samples used for the experiment for 304SS and 430SS was around 3.8 : 1, it can be calculated that approximately 74% of the H extracted from the target metal was stored at the counter electrode, showing a considerable efficiency. This can be an additional benefit where one can extract H out from the target alloy to prevent HE, and even store it in a H-storage material for later usage. It should be noted, however, that since the employed 304SS is not able to store a large amount of H due to its low H solubility, some H_2 bubbles could have formed at the interface and diffused out from the system. The 304SS counter electrode employed here simply illustrated the possibility of H storage, but the storage efficiency can be further improved by employing a H storage material as the counter electrode. Conductive H-storage materials such as magnesium alloys[55,56] or conducting polymers[57] could be potential candidates.

Conclusions

This study introduces a methodology aimed at electrochemically stimulating hydrogen removal to preventing hydrogen embrittlement in vital metallic alloys across diverse industries. This approach relies on a straightforward process involving the application of a cost-effective acid-in-clay electrolyte onto a metal component, followed by application of a positive potential. The findings illustrate that not only the hydrogen can be effectively extracted from the target metal, but it can also be stored in the counter electrode. The process can be further optimized for different steel grades, and operating conditions or requirements, and thus, constitutes a potential solution for hydrogen economy.

Experimental

Electrochemical treatments

H was electrochemically charged into the tensile samples in an aqueous solution of 5% H_2SO_4 + 3 g L^{-1} NH_4SCN with platinum wire as the counter electrode. A current density of -5 A m^{-2} was applied for 30 minutes for 430SS and one hour for low-carbon steel. Samples were rinsed with isopropanol afterwards. Sepiolite powder, 85% phosphoric acid and distilled water were mixed in a weight ratio of 1:3.76:1.18 and formed a gel-like solid electrolyte (details can be found in ref. 38). Three grams of this electrolyte was pasted on each of the two 304 grade austenitic stainless steel plates (20 mm × 30 mm), which were used as the counter electrodes. Then, the H-charged tensile sample was squeezed in between the two counter electrodes facing the surface pasted with the electrolyte. As mentioned, the electrolyte was in a gel-like state, forming an intact contact with the metal components. For ECD, a constant voltage of 0.3 V was applied, referencing our prior proof of principle study.[27] The samples were rinsed with isopropanol after the process. All processes were conducted at room temperature.

Tensile testing

Steel samples were cut into double-neck tensile specimens with gauge dimensions of 0.75, 1.3, and 4 mm of thickness, width, and length, respectively. The entire surface of the tensile samples was mechanically polished with 1200 grit sandpapers. Tensile tests were conducted with a Deben MTEST2000 mechanical testing system. The maximum strain rate of the system, 1.67×10^{-3} s^{-1}, was used to minimize H desorption during the tensile testing. Accurate strain values were measured by the digital image correlation method with speckle ink patterns dispersed on the gauge right before the tests. The interval between the electrochemical treatments and the tensile tests was equally controlled to be five minutes.

H permeation test

H permeation tests were conducted electrochemically at room temperature with a modified Devanathan–Stachurski permeation cell according to the ISO 17081 standard.[58] Thin plates were cut and polished down to 0.50 mm thickness, followed by final polishing with 1200 grit sandpapers. A 31.65 mm^2 circular area was exposed to electrolytes for both the H-charging and oxidation cells. The charging cell was filled with 30 g L^{-1} NaCl + 3 g L^{-1} NH_4SCN aqueous solution, and a current density of -5 A m^{-2} was applied. In the oxidation cell, 250 mV$_{SCE}$ was applied to the sample in 0.1 M NaOH solution. Pt wires were used as the counter electrode in both cells, and a Hg/HgO reference electrode was employed in the oxidation cell for voltage control. The effective H diffusivity was calculated by the breakthrough method:[58]

$$D_{eff} = \frac{L^2}{15.3 t_b}. \tag{1}$$

where L is the thickness of the sample, and t_b is the time where the oxidization current starts to increase.

Characterization

The characterization of the microstructure and fracture surfaces was conducted with a scanning electron microscope (SEM, TESCAN MIRA3) equipped with an electron back-scatter diffraction (EBSD) detector. The samples for EBSD measurement were prepared through mechanical polishing with colloidal silica. The roughness of the sample surface was measured with a confocal microscope (Sensofar Snoex) and calculated according to ISO 25178 standard.[51] The amount of total H in specimens was measured by the inert gas fusion method using a Horiba EMGA-830 ONH analyzer, calibrated with standard steel specimens with known H contents of 2.3 ± 0.4, 6.0 ± 0.5 wppm, respectively. The measurements were performed promptly within 60 s after the electrochemical processing and repeatedly with at least three specimens for each electrochemical treatment condition. The resistance values of the acid-in-clay electrolyte were measured using the 4-point probe method using CMT-SR2000N (Materials Development Corp). The acid-in-clay electrolyte was applied onto a non-conductive substrate to prevent any interference from external conductive surfaces.

Synchrotron XRD

Synchrotron transmission XRD measurements were conducted at the FAST beamline at the Cornell High Energy Synchrotron Source (CHESS). The X-ray beam used had an energy of 49.991 keV and a spot size of 0.5 × 0.5 mm. Two Dexela 2923 detectors captured the signals in three frames, each with a duration of 0.25 seconds. A CeO_2 standard was employed for instrument calibration. Prior to the measurements, a 0.5 mm thick 430 stainless steel sheet sample was H charged under identical parameters as above.

Author contributions

Conceptualization: K.-S. K., J. L., B. Y., and C. C. T. Funding acquisition, supervision and resources: J. L., B.Y., and C. C. T. Methodology: K.-S. K., J.-S. P., J. L., and C. C. T. Investigation and validation: K.-S. K., J.-S. P., Y.-C. Y., and J. K. Visualization: K.-S. K. Writing – original draft: K.-S. K. Writing – review and editing: K.-S. K., J. K., J. L., B. Y., and C. C. T.

Data availability

The data supporting this article have been included as part of the ESI.† Further data are available upon request from the authors.

Conflicts of interest

There are no conflicts to declare.

Acknowledgements

References

1 R. A. Oriani, *Annu. Rev. Mater. Sci.*, 1978, **8**, 327–357.

2 M. L. Martin, M. J. Connolly, F. W. DelRio and A. J. Slifka, *Appl. Phys. Rev.*, 2020, **7**, 041301.

3 P. Gong, A. Turk, J. Nutter, F. Yu, B. Wynne, P. Rivera-Diaz-del-Castillo and W. M. Rainforth, *Acta Mater.*, 2020, **223**, 117488.

4 J. R. Scully, G. A. Young and S. W. Smith, in *Gaseous Hydrogen Embrittlement of Materials in Energy Technologies*, ed. R. P. Gangloff and B. P. Somerday, Woodhead Publishing, 2012, pp. 707–768.

5 H. Zhao, P. Chakraborty, D. Ponge, T. Hickel, B. Sun, C.-H. Wu, B. Gault and D. Raabe, *Nature*, 2022, **602**, 437–441.

6 E. Tal-Gutelmacher and D. Eliezer, *JOM*, 2005, **57**, 46–49.

7 V. Madina and I. Azkarate, *Int. J. Hydrogen Energy*, 2009, **34**(14), 5976–5980.

8 X. Lu, Y. Ma and D. Wang, *Mater. Sci. Eng., A*, 2020, **792**, 139785.

9 G. Bertolino, G. Meyer and J. Perez Ipiña, *J. Alloys Compd.*, 2002, **330–332**, 408–413.

10 S. Kim, J.-H. Kang and Y. Lee, *J. Nucl. Mater.*, 2022, **559**, 153393.

11 X. Zhou, A. Tehranchi and W. A. Curtin, *Phys. Rev. Lett.*, 2021, **127**, 175501.

12 K. Ichii, M. Koyama, C. C. Tasan and K. Tsuzaki, *Scr. Mater.*, 2018, **150**, 74–77.

13 M. Safyari, M. Moshtaghi and S. Kuramoto, *Mater. Sci. Eng., A*, 2021, **799**, 139850.

14 M. D. Rowe, T. W. Nelson and J. C. Lippold, *Weld. J.*, 1999, **78**(2), 31s–37s.

15 T. Casanova, F. Soto, M. Eyraud and J. Crousier, *Corros. Sci.*, 1997, **39**(3), 529–537.

16 G. Jia, M. Lei, M. Li, W. Xu, R. Li, Y. Lu and M. Cai, *Int. J. Hydrogen Energy*, 2023, **48**, 32137–32157.

17 U.S. Department of Energy, U.S. National Clean Hydrogen Strategy and Roadmap, 2023, **https://www.hydrogen.energy.gov/clean-hydrogen-strategy-roadmap.html**, (accessed May 1, 2024).

18 S. K. Dwivedi and M. Vishwakarma, in *Advances in Manufacturing and Industrial Engineering*, ed. R. M. Singari, K. Mathiyazhagan and H. Kumar, Springer Nature, Singapore, 2021, pp. 673–683.

19 M. J. Robinson and R. M. Sharp, *Corrosion*, 1985, **41**(10), 582–586.

20 M. Koyama, C. C. Tasan and K. Tsuzaki, *Eng. Fract. Mech.*, 2019, **214**, 123–133.

21 W. M. Garrison and N. R. Moody, in *Gaseous Hydrogen Embrittlement of Materials in Energy Technologies*, ed. R. P. Gangloff and B. P. Somerday, Woodhead Publishing, 2012, pp. 421–492.

22 I. M. Robertson, P. Sofronis, A. Nagao, M. L. Martin, S. Wang, D. W. Gross and K. E. Nygren, *Metall. Mater. Trans. A*, 2015, **46**, 2323–2341.

23 H. Nishimura, T. Hojo, S. Ajito, Y. Shibayama, M. Koyama, H. Saitoh, A. Shiro, R. Yasuda, T. Shobu and E. Akiyama, *ISIJ Int.*, 2021, **61**(4), 1170–1178.

24 T. T. Nguyen, N. Tak, J. Park, S. H. Nahm and U. B. Baek, *Int. J. Hydrogen Energy*, 2020, **45**(43), 23739–23753.

25 P. Fassina, F. Bolzoni, G. Fumagalli, L. Lazzari, L. Vergani and A. Sciuccati, *Procedia Eng.*, 2011, **10**, 3226–3234.

26 D. Hardie and S. Liu, *Corros. Sci.*, 1996, **38**(5), 721–733.

27 J. Kim, X. Yao, D. Kong, J. Li, B. Yildiz and C. C. Tasan, *Appl. Mater. Today*, 2022, **29**, 101627.

28 J. Kim, J. Li, C. C. Taşan, X. Yao and B. Yildiz, PCT/US2021/43707, 2021.

29 K. Jiao, J. Xuan, Q. Du, Z. Bao, B. Xie, B. Wang, Y. Zhao, L. Fan, H. Wang, Z. Hou, S. Huo, N. P. Brandon, Y. Yin and M. D. Guiver, *Nature*, 2021, **595**, 361–369.

30 X. Wu, J. J. Hong, W. Shin, L. Ma, T. Liu, X. Bi, Y. Yuan, Y. Qi, T. W. Surta, W. Huang, J. Neuefeind, T. Wu, P. A. Greaney, J. Lu and X. Ji, *Nat. Energy*, 2019, **4**, 123–130.

31 C. S. Gittleman, H. Jia, E. S. De Castro, C. R. I. Chisholm and Y. S. Kim, *Joule*, 2021, **5**(7), 1660–1677.

32 L. Liu, W. Chen and Y. Li, *J. Membr. Sci.*, 2016, **504**, 1–9.

33 K. Hooshyari, M. Javanbakht, A. Shabanikia and M. Enhessari, *J. Power Sources*, 2015, **276**, 62–72.

34 V. Ramani, H. R. Kunz and J. M. Fenton, *J. Membr. Sci.*, 2004, **232**, 31–44.

35 P. Ramaswamy, N. E. Wonga and G. K. H. Shimizu, *Chem. Soc. Rev.*, 2014, **43**, 5913–5932.

36 R. Sahoo, S. Mondal, S. C. Pal, D. Mukherjee and M. C. Das, *Adv. Energy Mater.*, 2021, **11**(39), 2102300.

37 S. P. Nunes, B. Ruffmann, E. Rikowski, S. Vetter and K. Richau, *J. Membr. Sci.*, 2002, **203**(1–2), 215–225.

38 S. Wang, H. Jiang, Y. Dong, D. Clarkson, H. Zhu, C. M. Settens, Y. Ren, T. Nguyen, F. Han, W. Fan, S. Y. Kim, J. Zhang, W. Xue, S. K. Sandstrom, G. Xu, E. Tekoglu, M. Li, S. Deng, Q. Liu, S. G. Greenbaum, X. Ji, T. Gao and J. Li, *Adv. Mater.*, 2022, **34**(23), 2202063.

39 MaxGrip, Article: the cost of unplanned downtime, 2021, **https://www.maxgrip.com/resource/article-the-cost-of-unplanned-downtime/**, (accessed Aug 1, 2024).

40 M. A. Khan, C. Young and D. B. Layzell, The Techno-Economics of Hydrogen Pipelines, Transition Accelerator Technical Briefs, 2021, 1(2), 1-40, **https://transitionaccelerator.ca/reports/the-techno-economics-of-hydrogen-pipelines/**, (accessed May 1, 2024).

41 Interstate Natural Gas Association of America, Regulatory Treatment of Recoating Costs, 2007, **https://ingaa.org/regulatory-treatment-of-recoating-costs/**, (accessed May 1, 2024).

42 Indexbox, World – Clays – Market Analysis, Forecast, Size, Trends and Insights, 2024, **https://www.indexbox.io/store/world-clays-market-analysis-forecast-size-trends-and-insights,** (accessed May 1, 2024).

43 Chemanalyst, Phosphoric Acid Price Trend and Forecast, 2023, **https://www.chemanalyst.com/Pricing-data/phosphoric-acid-1162#:~:text=In%20the%20North%20American%20region, USD%201168%2FMT%20in%20March**, (accessed May 1, 2024).

44 D. Hardie, E. A. Charles and A. H. Lopez, *Corros. Sci.*, 2006, **48**(12), 4378–4385.

45 Y. Zhao, M.-Y. Seok, I.-C. Choi, Y.-H. Lee, S.-J. Park, U. Ramamurty, J.-Y. Suh and J.-I. Jang, *Scr. Mater.*, 2015, **107**, 46–49.

46 R. Kirchheim, *Scr. Mater.*, 2012, **67**(9), 767–770.

47 S. I. Rao, C. Woodward, B. Akdim and O. N. Senkov, *Materialia*, 2020, **9**, 100611.

48 K. Hirata, S. Iikubo, M. Koyama, K. Tsuzaki and H. Ohtani, *Metall. Mater. Trans. A*, 2018, **49**, 5015–5022.

49 M. Hashimoto and R. M. Latanision, *Acta Metall.*, 1988, **36**(7), 1837–1854.

50 M. Hashimoto and R. M. Latanision, *Metall. Mater. Trans. A*, 1988, **19**, 2789–2798.

51 ISO, ISO 25178-2: Geometrical product specifications (GPS)—Surface texture: Areal—Part 2: Terms, definitions and surface texture parameters, 2012.

52 T. Wang, X. Fang, H. Zhang, W. Lv, J. Ma, W. Liang and L. Zheng, *Mater. Lett.*, 2022, **313**, 131728.

53 M. B. Djukic, V. S. Zeravcic, G. Bakic, A. Sedmak and B. Rajicic, *Procedia Mater. Sci.*, 2014, **3**, 1167–11172.

54 Y. Lu, C.-Z. Zhao, H. Yuan, X.-B. Cheng, J.-Q. Huang and Q. Zhang, *Adv. Funct. Mater.*, 2021, **31**(18), 2009925.

55 A. Zaluska, L. Zaluski and J. O. Ström-Olsen, *J. Alloys Compd.*, 1999, **288**(1–2), 217–225.

56 L. Ouyang, F. Liu, H. Wang, J. Liu, X.-S. Yang, L. Sun and M. Zhu, *J. Alloys Compd.*, 2020, **832**, 154865.

57 N. Mahato, H. Jang, A. Dhyani and S. Cho, *Polymers*, 2020, **12**(11), 2480.

58 ISO, ISO 17081: Method of measurement of hydrogen permeation and determination of hydrogen uptake and transport in metals by an electrochemical technique, 2004.

Supplementary Information

Remove hydrogen and store it too: An acid-in-clay based electro-chemical solution

Kyung-Shik Kim,[a] Jin-Sung Park,[b] Young-Chul Yoon,[cd] Jinwoo Kim,[c] Ju Li,*[ab] Bilge Yildiz,*[ab] and Cemal Cem Tasan*[a]

[a] Department of Materials Science and Engineering, Massachusetts Institute of Technology, 77 Massachusetts Avenue, Cambridge, MA 02139, USA.

[b] Department of Nuclear Science and Engineering, Massachusetts Institute of Technology, 77 Massachusetts Avenue, Cambridge, MA 02139, USA.

[c] Energy Materials Research Center, Korea Institute of Science and Technology, Seoul 02792, Republic of Korea.

[d] Department of Materials Science and Engineering, Seoul National University, Seoul 08826, Republic of Korea.

*Corresponding author. Email: liju@mit.edu (J. Li), byildiz@mit.edu (B. Yildiz), tasan@mit.edu (C.C. Tasan)
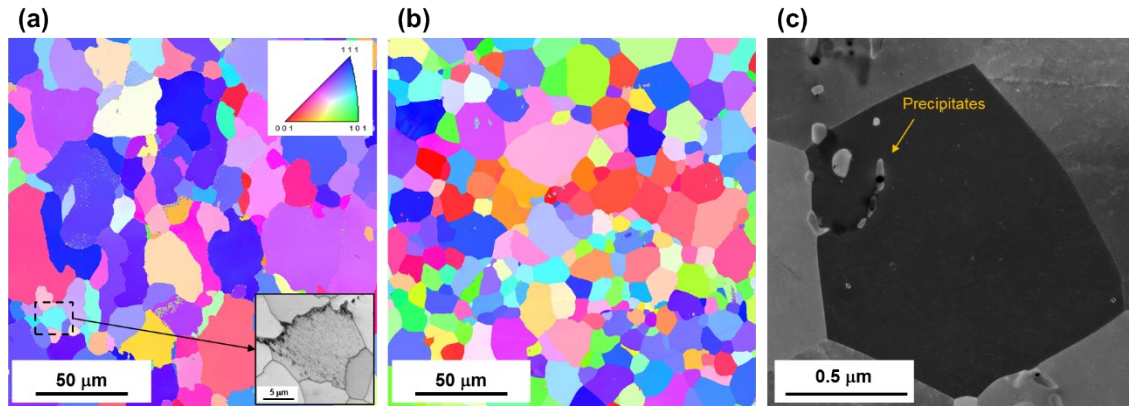
Contents:

Fig. S1 Microstructure of the investigated alloys. (a) EBSD inverse pole figure map of low-carbon steel showing ferrite with pearlite regions. (b) EBSD inverse pole figure map of 430 stainless steel. (c) BSE image of 430 stainless steel showing precipitates embedded inside ferrite matrix.
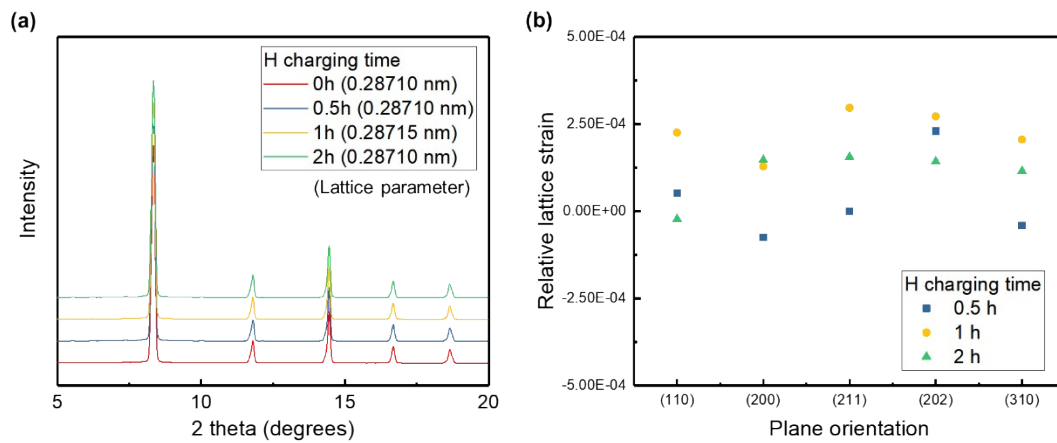

Fig. S2 Synchrotron XRD results after hydrogen charging. (a) Integrated intensity data with lattice parameter embedded in the legend. (b) Relative lattice strain for each plane orientation.
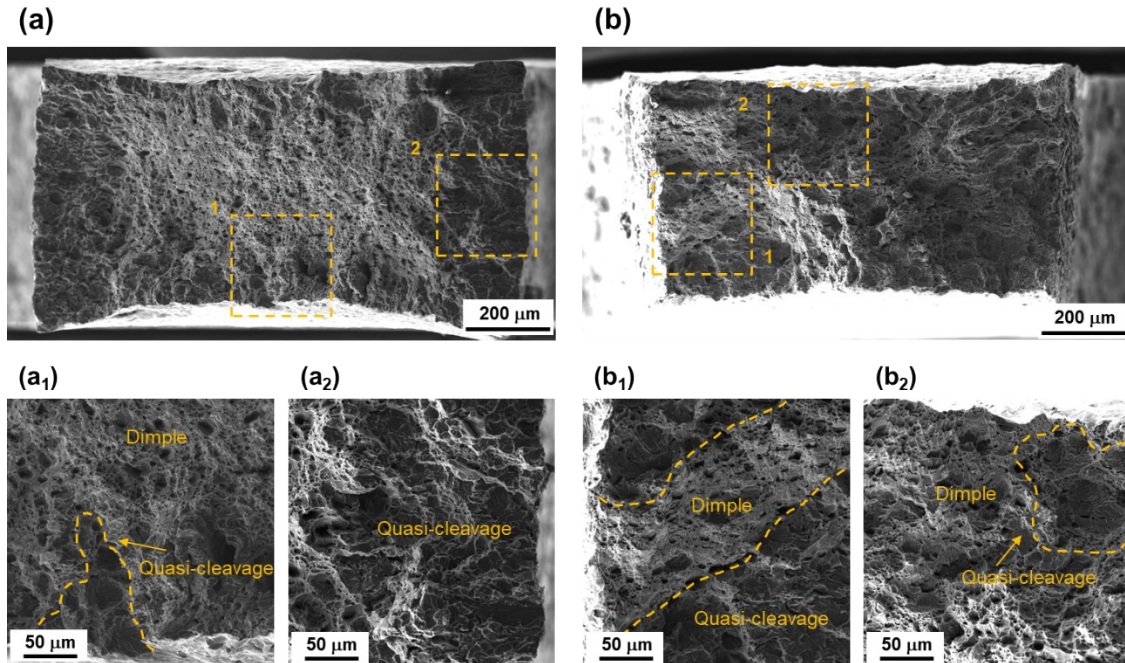
Fig. S3 Fractography of the tensile tested samples. (a) ECD treated for 30 minutes. (b) ECD treated for five hours. The figures below are the magnified images of the area marked in dotted boxes.
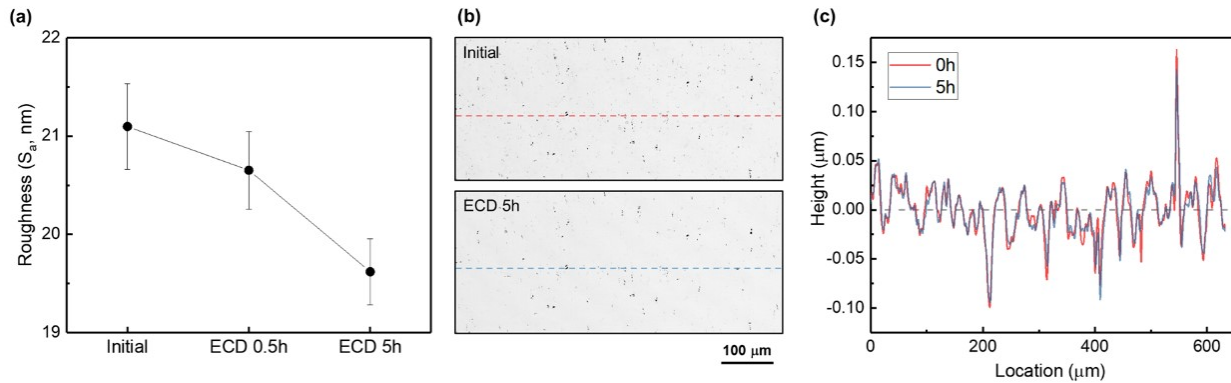

Fig. S4 Roughness measured before and after applying ECD treatment. (a) Change in roughness with increase in ECD treatment time. (b) Confocal images before and after applying 5 h of ECD. (c) Height profile measured before and after applying 5 h of ECD.
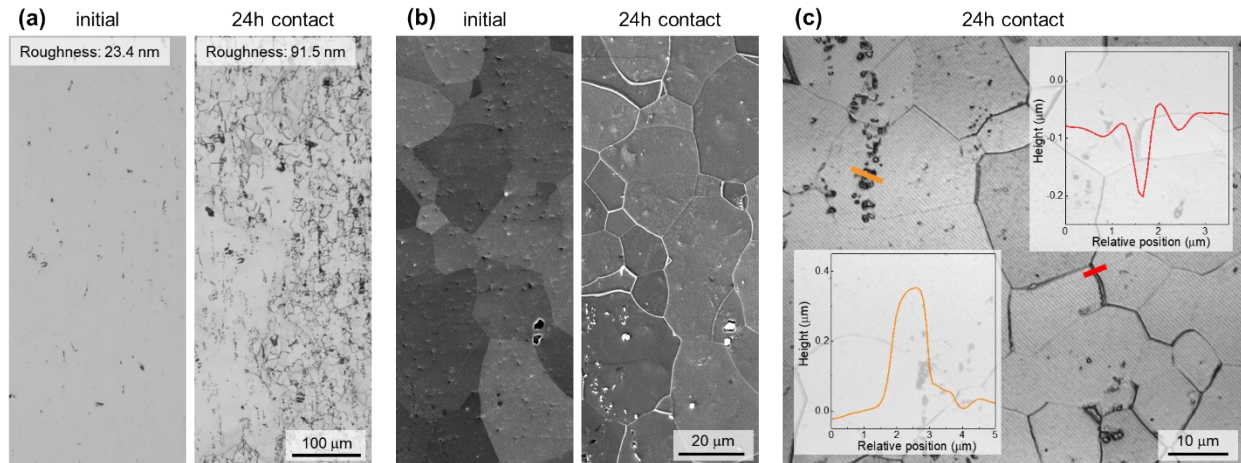
Fig. S5 Surface analysis before and after contacting acid-in-clay for 24 hours. (a) Overall optical image with roughness values (S_a) embedded on top left, (b) SEM secondary electron image, (c) confocal microscope images with height profile.
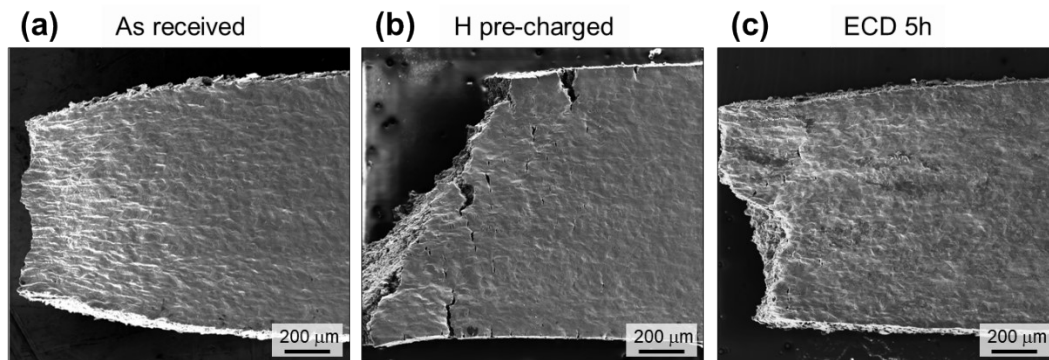

Fig. S6 Damage analysis of fractured tensile specimens. (a) Side surface view of the as-received sample near the fracture. (b) Hydrogen pre-charged sample. (c) ECD treated for five hours.
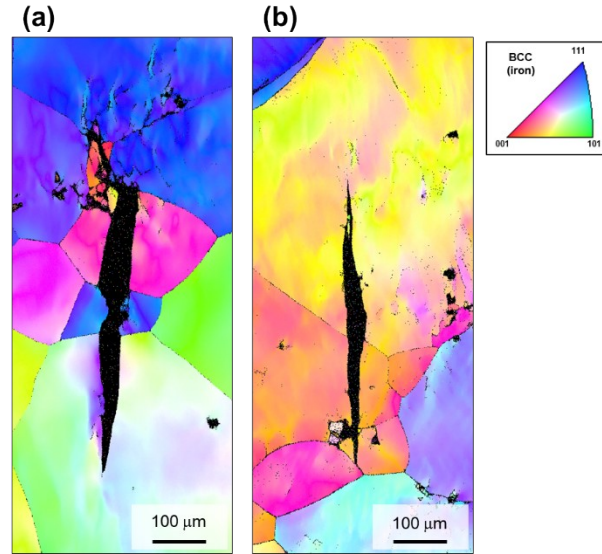
Fig. S7 EBSD inverse pole figure maps near cracks. (a) H pre-charged sample and (b) ECD 5 h treated sample after fracture.

	As received	H pre-charged	Air 0.5 h	Air 24 h	ECD 0.5 h	ECD 5 h
Fracture elongation (%)	37.6 ± 1.5	19.5 ± 0.5	19.8 ± 0.8	24.3 ± 0.1	24.0 ± 0.1	30.5 ± 1.5
Uniform elongation (%)	19.4 ± 0.1	14.1 ± 0.1	14.3 ± 0.3	16.4 ± 0.1	16.5 ± 0.4	19.0 ± 0.9
Yield strength (MPa)	314.1 ± 1.5	338.4 ± 2.3	336.6 ± 1.1	323.8 ± 5.3	320.8 ± 0.1	313.5 ± 1.9
Hydrogen content (wppm)	1.24 ± 0.83	7.70 ± 0.68	-	6.86 ± 0.28	-	3.31 ± 0.52

Table S1 Tensile properties and hydrogen content for each test conditions for 430 stainless steel.

	As received	H pre-charged	Air 1 h	Air 24 h	ECD 1 h	ECD 5 h
Fracture elongation (%)	55.2 ± 0.5	39.2 ± 0.3	41.4 ± 1.3	43.4 ± 0.8	52.4 ± 1.1	52.8 ± 3.2
Uniform elongation (%)	24.7 ± 1.4	16.1 ± 0.9	16.1 ± 0.2	18.2 ± 0.3	22.9 ± 0.8	23.5 ± 0.6
Yield strength (MPa)	190.7 ± 0.9	216.4 ± 4.9	199.6 ± 2.4	210.2 ± 5.2	187.2 ± 2.2	185.7 ± 2.6

Table S2 Tensile properties for each test conditions for low-carbon steel.